

Tailoring topological corner states in photonic crystals by near- and far-field coupling effects

Zhao-Jian Zhang(张兆健), Zhi-Hao Lan(兰智豪), Huan Chen(陈欢), Yang Yu(于洋), and Jun-Bo Yang(杨俊波)
Citation: Chin. Phys. B, 2023, 32 (**12**): 124201. DOI: 10.1088/1674-1056/acddd3
Journal homepage: http://cpb.iphy.ac.cn; http://iopscience.iop.org/cpb

What follows is a list of articles you may be interested in

Creation mechanism of electron-positron pair on equally spaced multiple localized fields

Chuan-Ke Li(李传可), Nan-Sheng Lin(林南省), Xian-Xian Zhou(周鲜鲜),Miao Jiang(江淼), and Ying-Jun Li(李英骏)
Chin. Phys. B, 2023, 32 (**9**): 094202. DOI: 10.1088/1674-1056/acd7cd

Microwave absorption and bandwidth study of Y_2Co_{17} rare earth soft magnetic alloy with easy-plane anisotropy

Yun-Guo Ma(马云国), Liang Qiao(乔亮), Zu-Ying Zheng(郑祖应), Hong-Bo Hao(郝宏波), Hao Wang(王浩), Zhe Sun(孙哲), Cheng-Fa Tu(涂成发), Tao Wang(王涛), Zheng Yang(杨正), and Fa-Shen Li(李发伸)
Chin. Phys. B, 2023, 32 (**8**): 084202. DOI: 10.1088/1674-1056/aca148

High-performance chiral all-optical OR logic gate based on topological edge states of valley photonic crystal

Xiaorong Wang(王晓蓉), Hongming Fei(费宏明), Han Lin(林瀚), Min Wu(武敏), Lijuan Kang(康丽娟), Mingda Zhang(张明达), Xin Liu(刘欣), Yibiao Yang(杨毅彪), and Liantuan Xiao(肖连团)
Chin. Phys. B, 2023, 32 (**7**): 074205. DOI: 10.1088/1674-1056/accb41

Quality factor enhancement of plasmonic surface lattice resonance by using asymmetric periods

Yunjie Shi(石云杰), Lei Xiong(熊磊), Yuming Dong(董玉明), Degui Sun(孙德贵), and Guangyuan Li(李光元)
Chin. Phys. B, 2022, 31 (**1**): 014217. DOI: 10.1088/1674-1056/ac1332

Optical properties of the two-port resonant tunneling filters in two-dimensional photonic crystal slabs

Ren Cheng (任承), Cheng Li-Feng (程立锋), Kang Feng (康凤), Gan Lin (甘霖), Zhang Dao-Zhong (张道中), Li Zhi-Yuan (李志远)
Chin. Phys. B, 2012, 21 (**10**): 104210. DOI: 10.1088/1674-1056/21/10/104210

Tailoring topological corner states in photonic crystals by near- and far-field coupling effects

Zhao-Jian Zhang(张兆健)[1,2,†], Zhi-Hao Lan(兰智豪)[3], Huan Chen(陈欢)[1,2], Yang Yu(于洋)[1,2], and Jun-Bo Yang(杨俊波)[1,2,‡]

[1] *Department of Physics, National University of Defense Technology, Changsha* 410073, *China*
[2] *Center of Material Science, National University of Defense Technology, Changsha* 410073, *China*
[3] *Department of Electronic and Electrical Engineering, University College London, London WC1E* 7*JE, United Kingdom*

(Received 22 May 2023; revised manuscript received 3 June 2023; accepted manuscript online 13 June 2023)

We explore the behaviors of optically coupled topological corner states in supercell arrays composed of photonic crystal rods, where each supercell is a second-order topological insulator. Our findings indicate that the coupled corner states possess nondegenerate eigenfrequencies at the Γ point, with coupled dipole corner states excited resonantly by incident plane waves and displaying a polarization-independent characteristic. The resonance properties of coupled dipole corner states can be effectively modulated via evanescently near-field coupling, while multipole decomposition shows that they are primarily dominated by electric quadrupole moment and magnetic dipole moment. Furthermore, we demonstrate that these coupled corner states can form surface lattice resonances driven by diffractively far-field coupling, leading to a dramatic increase in the quality factor. This work introduces more optical approaches to tailoring photonic topological states, and holds potential applications in mid-infrared topological micro-nano devices.

Keywords: topological corner states, photonic crystal slabs, optical coupling effects, surface lattice resonances

PACS: 42.25.Bs, 42.60.Da, 42.55.Tv **DOI:** 10.1088/1674-1056/acddd3

1. Introduction

With the advent of the intersection between topology and photonics, the research of topological photonics has offered new approaches to understanding and manipulating the behavior of light in micro-nano structures.[1,2] Over the past decade, a variety of platforms have been established to realize topological photonics, including photonic crystals (PhCs), metamaterials, and waveguide lattices.[3–5] Among these platforms, topological PhCs have received significant attention due to the straightforward analogue to solid state systems and the feasibility of on-chip integrated optical systems.[6] For example, topological valley-dependent edge states were introduced into PhC hole slabs to realize electromagnetic wave propagation with backscattering suppression, which could be applied to robust data transmission in the telecommunication and terahertz bands,[7–9] and even to quantum information processing.[10] Besides, higher-order topological insulators were further proposed recently,[11] where two-dimensional (2D) second-order topological insulators (SOTIs) could support localized corner states and serve as optical nanocavities with high quality (Q) factors in PhCs.[12,13] On this basis, several topological applications have been implemented, such as topological lasing and strong coupling.[14,15]

Meanwhile, metasurfaces, the 2D counterparts of metamaterials, were also introduced into topological photonics.[16] One example was the topological metasurface based on patterned graphene, which can support edge plasmons that enhance the four-wave mixing nonlinear process.[17] Plasmonic metal metasurfaces could also be used for electrically active control of topological microwave transport.[18] Especially, it is natural to pay more attention to the optical coupling effect between topological states, since it is one of the most important features occurring in metasurfaces. Through arranging meta-atoms periodically, it was inevitable to include optical evanescent coupling between adjacent meta-atoms, which will regulate optical properties of resonances supported on meta-atoms.[19] On the other hand, diffractively far-field coupling could also exist in metasurfaces, leading to surface lattice resonance (SLR) with spectral narrowing.[20] Recent studies have investigated by using coupling effects to tailor the optical properties of photonic topological states through periodically arranging PhC supercells like metasurfaces, namely, PhC supercell arrays, where each supercell is SOTI.[21,22] Interestingly, these corner states exhibit exotic characteristics such as nondegenerate eigenfrequencies and collective behaviors,caused by near-field coupling. Moreover, such arrays provide a versatile platform for studying the topological light-matter interaction,[23] having potential applications in large-area topological photonic devices. However, these studies have involved only PhC hole slabs so far, where another typical PhC slab, the rod slab, is still missing. In addition, the influence of far-field coupling in corner states has remained

[†]Corresponding author. E-mail: zhangzhaojian@nudt.edu.cn
[‡]Corresponding author. E-mail: yangjunbo@nudt.edu.cn

© 2023 Chinese Physical Society and IOP Publishing Ltd

unclear up to now.

In this work, we extend the theoretical investigation of coupled corner states in supercell arrays to PhC rod slab frameworks. Following 2D Su–Schrieffer–Heeger (SSH) model, we construct SOTIs by surrounding topologically nontrivial unit cells with trivial ones, which are then arranged periodically to form the supercell array. This results in the coupling of multipole corner states in neighboring SOTIs, which are located above the light line and accessible to external excitation. Our eigenmode analysis demonstrates that there are three types of coupled corner states with nondegenerate eigenfrequencies at Γ point, while full-wave simulation reveals that coupled dipole corner states can be excited as resonances with polarization insensitivity. We further illustrate that the resonant wavelength and Q factor of the coupled corner state can be effectively tuned through the adjustment of inter- and intra-supercell near-field coupling. In addition, our multipole decomposition calculation reveals the electric quadrupole (EQ) and magnetic dipole (MD) nature of coupled corner states, which distinguish them from those supported in supercell arrays based on PhC hole slab structures. Finally, we observe a sharp increase in Q factor and a unique spectral profile as the resonant wavelength of the coupled corner states approaches to the Rayleigh anomaly (RA) position via increasing the surrounding refractive index (SRI), suggesting the emergence of SLRs induced by far-field coupling. This work introduces more optical means for the customization of corner states in PhCs, and has the potential to be applied to mid-infrared topological lasers, sensors, and detectors.

2. Structure and method

Figure 1(a) shows the geometrical configuration of the topological supercell array. It includes periodically arranged supercells based on PhC rod slab structures surrounded by air, and each supercell is an SOTI,[24] consisting of a square topological nontrivial region (highlighted in blue) surrounded with a trivial region (highlighted in green). The trivial region and nontrivial region are composed of trivial/nontrivial unit cells with four compact dielectric rod and expanded dielectric rods, whose lattice constant $a = 2.03$ μm, height $h = 2a$, and permittivity $\varepsilon = 16$ (corresponding to germanium in mid-infrared[25]). Additionally, m and n represent the number of rows of trivial unit cells between neighboring nontrivial regions, and the number of rows of nontrivial unit cells within one supercell, respectively, thus the period of the supercell $P = a(m+n)$. By varying m or n, we can separately tune the evanescently optical interaction between corner states located in adjacent supercells or the same supercell respectively, namely, the inter-supercell coupling and intra-supercell coupling respectively.

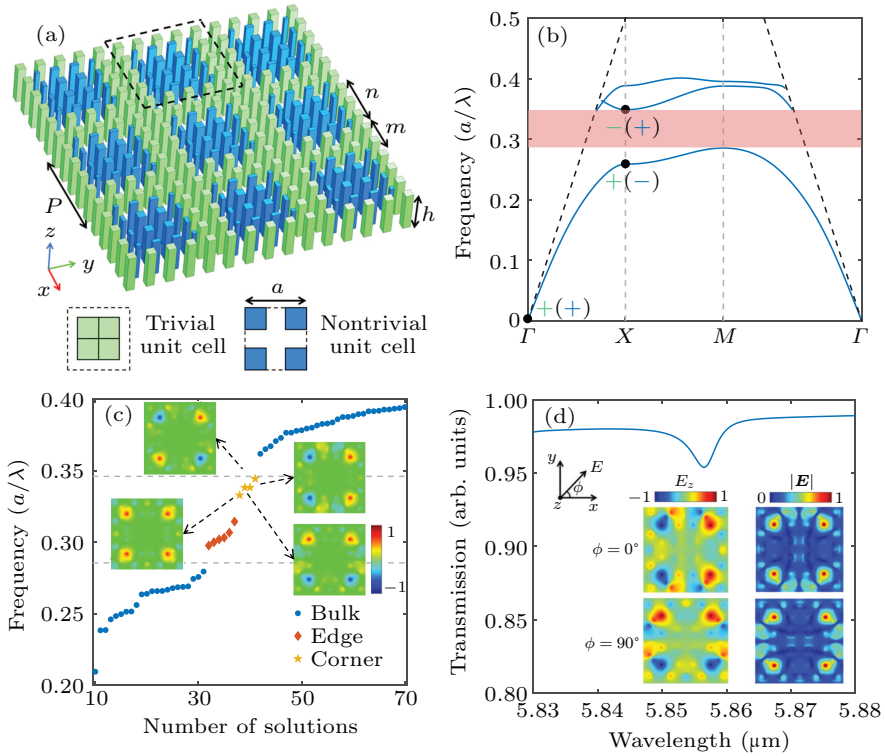


Fig. 1. (a) Schematic diagram of supercell array. Each supercell is comprised of nontrivial unit cells surrounded by trivial unit cells. Insets present schematics of unit cells that possess four compact or expanded dielectric rods with a side length of $0.2a$, respectively. (b) Bands of nontrivial and trivial unit cells. The symbols + and − indicate even parity and odd parity of modes at high-symmetry points, respectively, where green and blue colors represent trivial and nontrivial cases, respectively. (c) Eigenmodes of the supercell array at the Γ point when $m = 2$ and $n = 3$. The gray dashed lines indicate the band gap of the unit cell. Insets show E_z profiles of eigenmodes in each supercell. (d) Transmission spectrum of the supercell array under plane waves with polarization angle ϕ, where ϕ is defined in the inset. Insets also show E_z and $|\boldsymbol{E}|$ fields at the resonance in each supercell under different values of ϕ.

In Fig. 1(b), we present the first three photonic bands of trivial unit cell and nontrivial unit cells, which is calculated via plane-wave expansion (PWE) method. Here, we only consider transverse magnetic (TM) modes below the light line since rods favor TM band gaps.[5] It is shown that the two unit cells possess identical band structures, and there exists a band gap between the first band and the second band. The topological properties of the two unit cells can be distinguished by 2D Zak phase $\theta = (\theta_x, \theta_y)$, which is determined by the field parity at Γ and X (Y) points as[26]

$$\theta_\alpha = \pi \left(\sum_i q_\alpha^i \bmod 2 \right),$$
$$(-1)^{q_\alpha^i} = \frac{\eta(X_\alpha)}{\eta(\Gamma)}, \quad \alpha = x, y. \tag{1}$$

Here, X_α is X or Y point for $\alpha = x$ or y, respectively, η denotes the parity of field at high-symmetry point with respect to the middle plane at $\alpha = a/2$, and i runs over all the bands below the gap, which only involves the first band in this case. Owing to C_4 symmetry of the unit cell, we also have $\theta_x = \theta_y$. For trivial unit cell, we find that its fields of the first band possess even parity at both Γ point and X point as indicated by symbol $+$ in green in Fig. 1(b), thus it possesses 2D Zak phase (0,0), namely, a topologically trivial phase. For nontrivial unit cell, it has nontrivial 2D Zak phase (π, π) since its parity at X point becomes odd as indicated by symbol $-$ in blue in Fig. 1(b). Such a parity reversal is attributed to the band inversion between the first two bands during the topological phase transition process.[21]

3. Results and discussion

Then we turn to the investigation of the supercell array with $m = 2$ and $n = 3$ as given in Fig. 1(a). Since we only consider the case of normal incidence in this work, the eigenmodes of the periodic supercells at Γ point are calculated, and the results are shown in Fig. 1(c). It is shown that there are six coupled edge states and four coupled corner states within the band gap of the unit cell, and we focus on the latter. Their field distributions of the E_z component, determined in the x–y plane of the supercell at the middle of the slab ($z = h/2$), are presented in the insets of Fig. 1(c). These plots show that electric fields of coupled corner states are tightly localized in four corners of the nontrivial region, and exhibit characteristics of multipole corner states defined by Kim *et al.*,[27] namely, monopole, dipole I, dipole II, and quadrupole corner states from low to high frequencies. Especially, different types of coupled corner states possess nondegenerate eigenfrequencies owing to near-field evanescent coupling, which is a unique feature that distinguishes them from conventional corner states in isolated SOTIs. However, the degeneracy of the two coupled dipole corner states remains unbroken.

These coupled corner states are beyond the light line at Γ point of the supercell array, thus they are radiative and accessible to external excitation. We perform the full-wave simulation of the supercell array based on finite-difference time-domain (FDTD) method, where one supercell is modeled under the periodic boundary condition in the x direction and y direction and a plane wave source is introduced on the top with normal incidence for far-field excitation. The transmission spectrum is shown in Fig. 1(d), which shows a resonant dip at 5.857 μm, corresponding to the eigenfrequency of coupled dipole corner states. Field distributions at the resonant wavelength also exhibit features of coupled dipole corner states as shown in plots of Fig. 1(d), confirming that they are excited as resonances. Owing to the C_4 symmetry of the supercell array, the spectral response of coupled dipole corner states is insensitive to the polarization angle ϕ of the plane wave. Especially, different coupled dipole corner states can be selectively excited by tuning the polarization angle as shown in plots of Fig. 1(d). Notably, there is no spectral evidence of coupled monopole and quadrupole corner states, since they cannot be directly stimulated by the source due to the symmetry mismatch, namely, there is no overlap between their fields and the plane waves. We will keep $\phi = 0$ in the following discussion.

The transmission spectrum of coupled dipole corner states can be fitted by the following Fano formula:[28]

$$T_{\text{Fano}} = \left| a_1 + \mathrm{i}a_2 + \frac{b}{\omega - \omega_0 + \mathrm{i}\gamma} \right|^2, \tag{2}$$

where a_1, a_2, and b denote constant real parameters, ω_0 is the resonant frequency, and γ refers to the damping rate of the resonance. The Q factor of the resonance can be calculated from the relation $Q = \omega_0/(2\gamma)$. In this case, coupled dipole corner states possess a low Q factor of 1252, and thus we further examine the near-field coupling effect for enhancing the resonance performance of coupled dipole corner states. By varying m and n, the inter-supercell and intra-supercell coupling effects are investigated, and the corresponding transmission spectra are shown in Fig. 2, where the positions of coupled dipole corner states are indicated by arrows. It is shown that these near-field couplings can alter the resonance properties of coupled dipole corner states effectively. For example, if we maintain $n = 3$ and increase the inter-supercell coupling strength by reducing m, the resonant wavelength and Q factor of coupled dipole corner state can be modified as shown in Fig. 2(b), and a Q factor of 3389 can be obtained at 5.934 μm when $m = 1$. Similarly, if comparing the transmission spectra of different values of n with the same m (shown by curves with the same color in Fig. 2), one can find that the intra-supercell coupling also plays an important role in determining the resonance behaviors of coupled dipole corner states. Especially, coupled dipole corner states reach a high Q factor of 1.68×10^4 at 5.892 μm when $m = n = 2$ as depicted in Fig. 2(c).

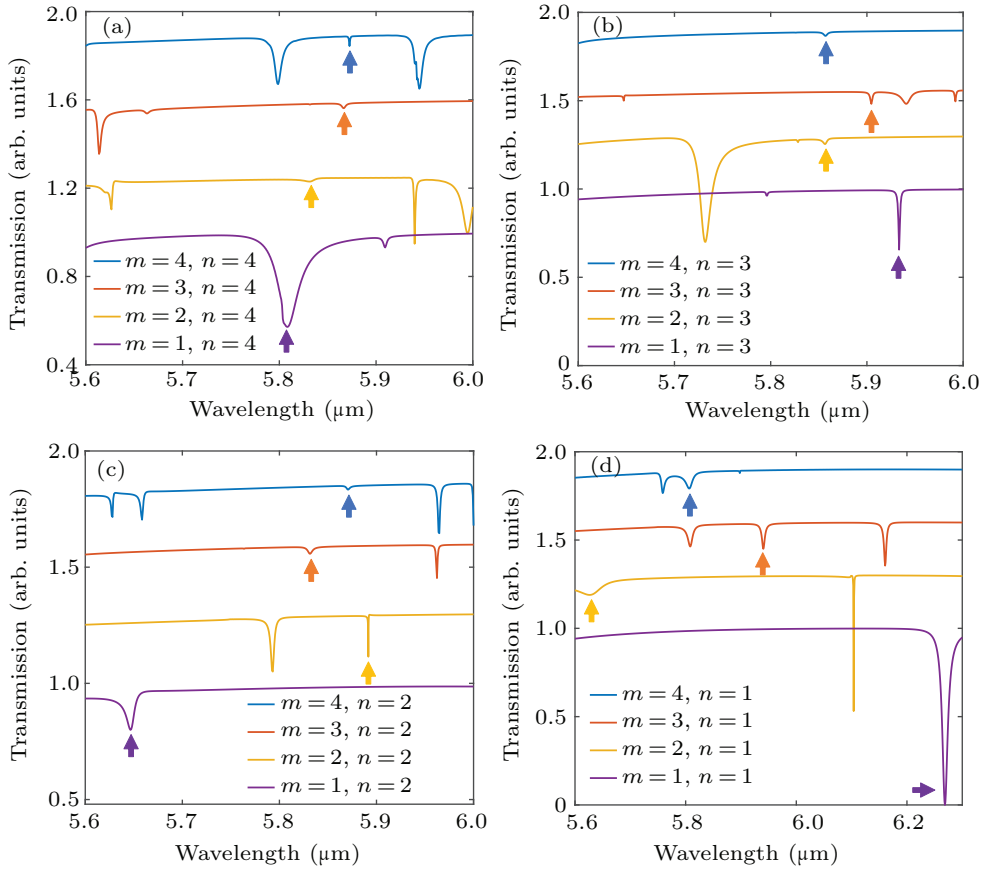


Fig. 2. (a)–(d) Transmission spectra of the supercell array at different values of m and n, with arrows indicating positions of coupled dipole corner states.

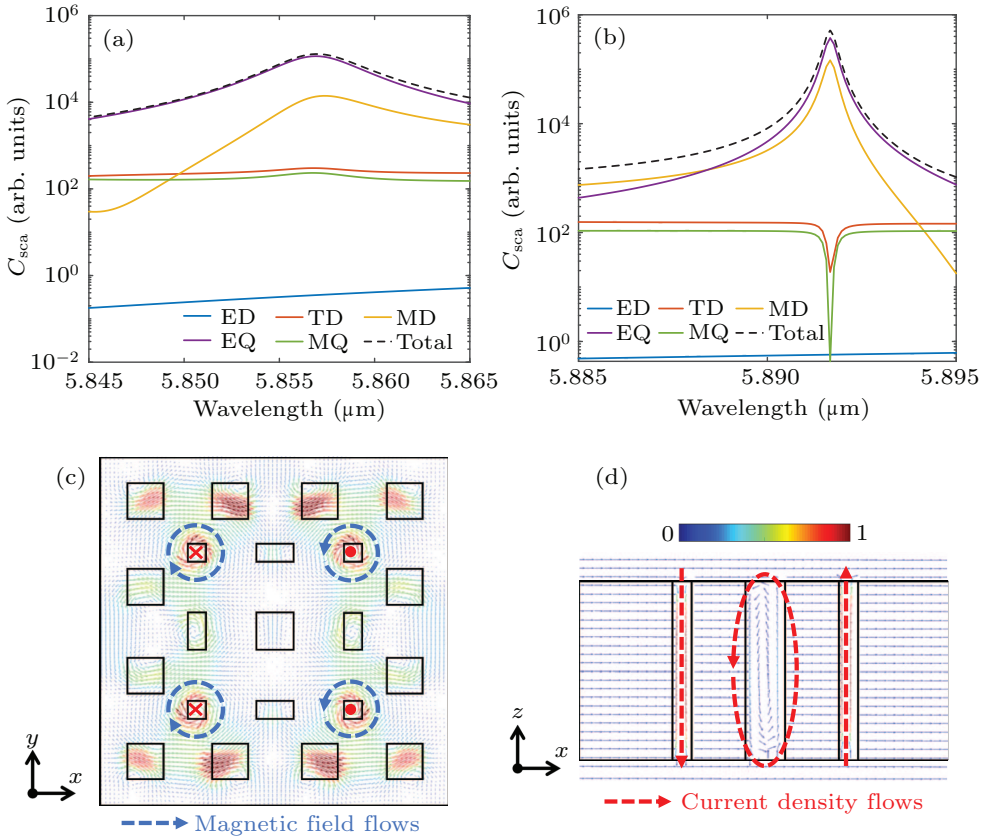


Fig. 3. (a) Multipolar scattering cross-sections of coupled dipole corner states when (a) $m = 2$ and $n = 3$; (b) $m = n = 2$. (c) Magnetic field vectors of coupled dipole corner states when $m = n = 2$. Colors of vectors indicate the corresponding normalized magnitudes, blue arrows indicate flows of magnetic fields, and the red circle and cross indicate directions of displacement currents. (d) Displacement current density of coupled dipole corner states. Red arrows indicate their flows.

To gain more insights into coupled dipole corner states, we perform the multipole decomposition under the Cartesian coordinate system.[29] Here, we consider two cases of coupled dipole corner states, the first being $m = 2$ and $n = 3$, and the second being $m = n = 2$. The corresponding multipolar scattering cross-section $C_{\rm sca}$, including electric dipole (ED), toroidal dipole (TD), MD, EQ, and magnetic quadrupole (MQ), is presented in Figs. 3(a) and 3(b), respectively. It is shown that coupled dipole corner states in both cases are dominated by EQ and MD, where MD is slightly weaker than EQ. Further investigations reveal that the coupled dipole corner states are always dominated by EQ and MD in other m–n cases. To exhibit the origin of the multipoles, the magnetic field vectors in the x–y middle plane of the supercell with $m = n = 2$ are visualized in Fig. 3(c). It is shown that the magnetic field vectors circulate clockwise around the left corners, while counterclockwise around right corners as indicated by the blue arrows. They also generate a pair of EDs with opposite phases as indicated by the red circles and crosses. Figure 3(d) shows the displacement current density in the x–z cross-section of lower corners, confirming the formation of EDs as indicated by the red dashed straight arrows. Thus, these EDs with opposite phases form the EQ response. Meanwhile, the current loop appearing in Fig. 3(d) is attributed to the MD response. Interestingly, these coupled dipole corner states show completely different multipole natures from those in PhC hole slabs, where coupled dipole corner states are dominated by TD and MQ.[22] Therefore, although coupled dipole corner states share the same topological origin (the topological charge) in PhC rod and hole slabs, their natures in real space will differ. This is due to the fact that their in-plane topologically enforced circular flows are caused by magnetic fields and electric currents, respectively.

Owing to the high Q-factor of coupled dipole corner states when $m = n = 2$, we further investigate the diffractively far-field coupling effect in this case to see whether the Q factor can be further improved. In the metasurfaces, the localized resonances in individual micro-nano particles can be coupled with in-plane diffracted propagating waves, leading to the SLRs with narrower linewidth. In principle, the SLRs can also exist in any other periodic optical structures such as PhC slabs. In this work, the spectral position of SLR under the normal incidence is determined by the following RA equation:

$$\lambda_{\rm r}(i,j) = \frac{n_{\rm s}P}{\sqrt{i^2+j^2}}, \tag{3}$$

where $n_{\rm s}$ is the SRI around the array, P is the period of the supercell, and (i, j) is the diffraction order of the RAs.

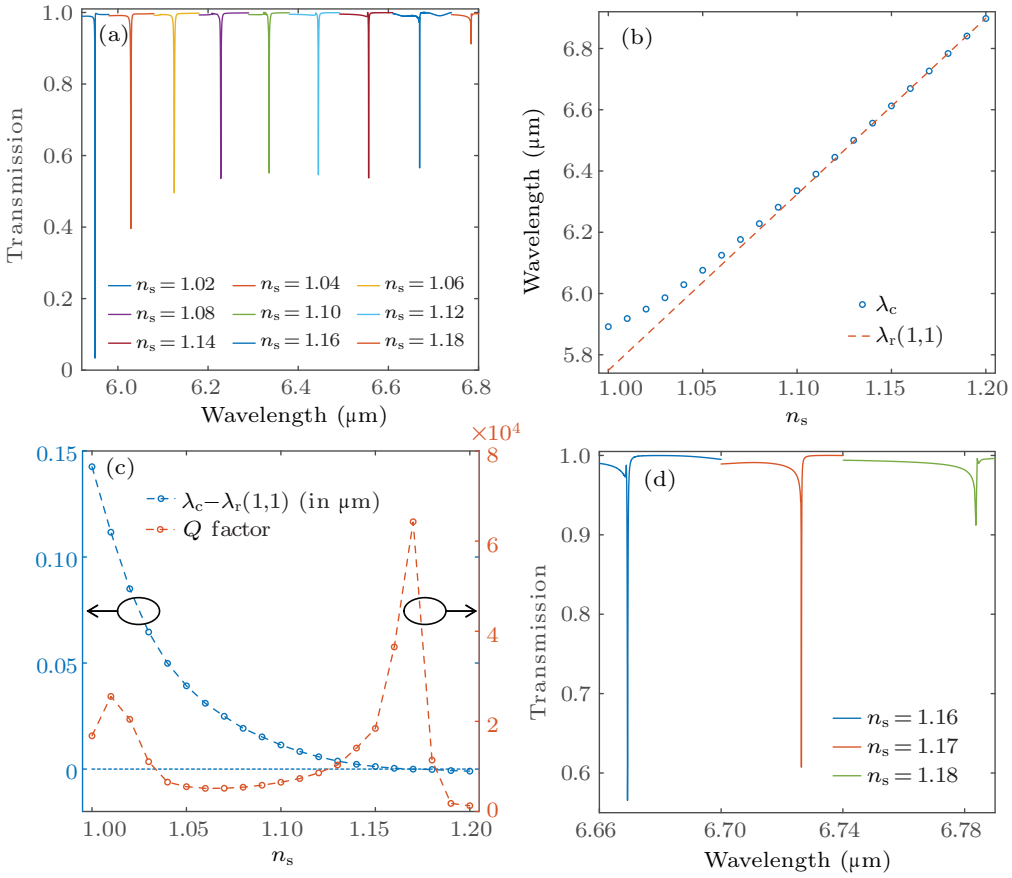


Fig. 4. (a) Transmission spectra of supercell array under different SRIs. (b) Wavelength of coupled dipole corner state and RA at (1,1) under different SRIs. (c) Difference between two wavelengths and Q factor of coupled dipole corner state under different SRIs. (d) Transmission spectra of supercell array when SRI is 1.16, 1.17, and 1.18.

Although the current resonant wavelength of coupled dipole corner state λ_c does not match any λ_r, for theoretical investigation, we can assume that the structure is surrounded by a homogenous lossless medium, and slightly vary the SRI to make the two wavelength positions overlap, since they have different dispersive behaviors with the SRI. Figure 4(a) shows transmission spectra of coupled dipole corner states under different SRIs, exhibiting that the resonant wavelength will redshift with increasing SRI, and the corresponding Q factor is also modified simultaneously. Figure 4(b) displays the relationship of wavelength versus n_s for λ_c and λ_r (at the diffraction order (1,1)), respectively, with the SRI, which shows that the two curves becomes closer as the SRI increases. In Fig. 4(c), we further present the difference between λ_c and $\lambda_r(1,1)$, and the Q factor of coupled dipole corner state, under different SRIs. It is evident that the two wavelengths exponentially approach to each other as the SRI increases, and when they coincide at $n_s = 1.17$ (the position is indicated by the blue dashed line), the Q factor dramatically increases up to 6.43×10^4. The transmission spectra near the high-Q regime are plotted in Fig. 4(d), which exhibit typical spectral profiles of SLRs, including small transmission peaks caused by diffraction next the main transmission dips at $n_s = 1.16$ and 1.18, and the much narrower transmission dip resulting from the diffraction at $n_s = 1.17$. The above features all indicate the occurrence of SLRs caused by the far-field coupling, which further enrich the optical approaches to tailoring the resonance properties of coupled dipole corner states.

4. Conclusions

In summary, we theoretically investigated the optical properties of coupled corner states in the supercell array based on PhC rod slabs. The eigenmode analysis shows the non-degenerate features of multipole coupled corner states, and the full-wave simulation reveals the accessibility of coupled dipole corner states by using the plane-wave stimulation, which exhibits polarization-independent resonance characteristics. The resonant wavelength and Q factor of coupled dipole corner states can be effectively tuned by inter-supercell near-field coupling effect and intra-supercell near-field coupling effect, and the multipole decomposition reveals that coupled dipole corner states are dominated by the EQ and MD, which is completely different from the scenario in PhC hole slabs. Finally, by varying the SRI, the Q factor of coupled dipole corner state is further improved through matching the RA position of the structure, namely, forming the SLRs caused by diffractively far-field coupling effects. In practice, the array can be fabricated on germanium-on-insulator platforms.[30] The photoresist should be first deposited on the top surface, and patterns of PhCs can be written with electron beam lithography. Then, the patterns can be transferred into the top germanium layer by using reactive ion etching techniques.[31] Although the insulator (silica) substrate will introduce asymmetric environment, the corresponding low RI will only cause a slight shift at the resonant wavelength, and the physical mechanism introduced in this work still holds.[7–10,32] This work reveals that compared with conventional isolated corner states, coupled corner states possess rich optical phenomena and many degrees of freedom to control, and such topological supercell arrays have potential applications in mid-infrared lasing, sensing, and detection.

Acknowledgements

Project supported by the National Natural Science Foundation of China (Grant Nos. 62275271, 12272407, and 62275269), the National Key Research and Development Program of China (Grant No. 2022YFF0706005), the Natural Science Foundation of Hunan Province, China (Grant Nos. 2023JJ40683, 2022JJ40552, and 2020JJ5646), and the Program for New Century Excellent Talents in University, China (Grant No. NCET-12-0142).

References

[1] Lu L, Joannopoulos J D and Soljačić M 2014 *Nat. Photon.* **8** 821
[2] Ozawa T, Price H M, Amo A, Goldman N, Hafezi M, Lu L, Rechtsman M C, Schuster D, Simon J, Zilberberg O and Carusotto I 2019 *Rev. Mod. Phys.* **91** 015006
[3] Chen J and Li Z Y 2022 *Chin. Phys. B* **31** 114207
[4] Ma S, Yang B and Zhang S 2022 *Photon. Insights* **1** R02
[5] Lan Z, Chen M, Gao F, Zhang S and Sha Wei E I 2022 *Rev. Phys.* **9** 100076
[6] Tang G J, Chen X D and Dong J N 2019 *Physics* **48** 376 (in Chinese)
[7] He X T, Liang E T, Yuan J J, Qiu H Y, Chen X D, Zhao F L and Dong J W 2019 *Nat. Commun.* **10** 872
[8] Shalaev M I, Walasik W, Tsukernik A, *et al.* 2019 *Nat. Nanotechnol.* **14** 31
[9] Yang Y H, Yamagami Y, Yu X B, Pitchappa P, Webber J, Zhang B L, Fujita M, Nagatsuma T and Singh R 2020 *Nat. Photon.* **14** 446
[10] Chen Y, He X T, Cheng Y J, Qiu H Y, Feng L T, Zhang M, Dai D X, Guo G C, Dong J W and Ren X F 2021 *Phys. Rev. Lett.* **126** 230503
[11] Wang H F, Xie B Y, Zhan P, Lu M H and Chen Y F 2019 *Acta Phys. Sin.* **68** 224206 (in Chinese)
[12] Ota Y, Liu F, Katsumi R, Watanabe K, Wakabayashi K, Arakawa Y and Iwamoto S 2019 *Optica* **6** 786
[13] He X T, Li M Y, Qiu H Y, Ruan W S, Zhou L D, Liu L, Chen X D, Chen W J, Zhao F L and Dong J W 2021 *Photon. Res.* **9** 1423
[14] Zhang W, Xie X, Hao H, Dang J, Xiao S, Shi S, Ni H, Niu Z, Wang C, Jin K, Zhang X and Xu X 2020 *Light: Sci. Appl.* **9** 109
[15] Zhang H, Zheng Y, Yu Z M, Hu X and Lu C 2021 *J. Opt.* **23** 124002
[16] You J W, Lan Z, Ma Q, Gao Z, Yang Y, Gao F, Xiao M and Cui T J 2023 *Photon. Res.* **11** B65
[17] You J W, Lan Z and Panoiu N C 2020 *Sci. Adv.* **6** eaaz3910
[18] You J W, Ma Q, Lan Z, Xiao Q, Panoiu N C and Cui T J 2021 *Nat. Commun.* **12** 1
[19] Pu M B, Wang C T, Wang Y Q and Luo X G 2017 *Acta Phys. Sin.* **66** 144101 (in Chinese)
[20] Kravets V G, Kabashin A V, Barnes W L and Grigorenko A N 2018 *Chem. Rev.* **118** 5912
[21] Zhang Z, You J W, Lan Z and Panoiu N C 2021 *J. Opt.* **23** 095102
[22] Zhang Z, Yang J, Du T, Ma H and Jiang X 2022 *Opt. Lett.* **47** 1642

[23] Zhang Z, Yang J, Du T and Jiang X 2022 *Photon. Res.* **10** 855

[24] Xie B Y, Wang H F, Wang H X, Zhu X Y, Jiang J H, Lu M H and Chen Y F 2018 *Phys. Rev. B* **98** 205147

[25] Amotchkina T, Trubetskov M, Hahner D and Pervak V 2020 *Appl. Opt.* **59** A40

[26] Liu F and Wakabayashi K 2017 *Phys. Rev. Lett.* **118** 076803

[27] Kim H R, Hwang M S, Smirnova D, Jeong K Y, Kivshar Y and Park H G 2020 *Nat. Commun.* **11** 5758

[28] Limonov M F, Rybin M V, Poddubny A N and Kivshar Y S 2017 *Nat. Photon.* **11** 543

[29] Alaee R, Rockstuhl C and Fernandez-Corbaton I 2018 *Opt. Commun.* **407** 17

[30] El Kurdi M, David S, Checoury X, Fishman G, Boucaud P, Kermarrec O, Bensahel D and Ghyselen B 2008 *Opt. Commun.* **281** 846

[31] Jiang L, Jia W, Zheng G and Li X 2012 *Opt. Lett.* **37** 1424

[32] Lu C, Sun Y Z, Wang C, Zhang H, Zhao W, Hu X, Xiao M, Ding W, Liu Y C and Chan C T 2022 *Nat. Commun.* **13** 2586